Structural landscape of the Respiratory Syncytial Virus nucleocapsids

Lorène Gonnin, Ambroise Desfosses, Maria Bacia-Verloop, Didier Chevret, Marie Galloux, Jean-François Éléouët, Irina Gutsche

Structural landscape of the Respiratory Syncytial Virus nucleocapsids

Lorène Gonnin[1,2], Ambroise Desfosses[1,*], Maria Bacia-Verloop[1], Didier Chevret[2], Marie Galloux[2], Jean-François Éléouët[2] and Irina Gutsche[1,*]

Affiliations

[1]Institut de Biologie Structurale, Univ Grenoble Alpes, CEA, CNRS, IBS, 71 Avenue des martyrs, F-38044 Grenoble, France

[2]VIM, Paris-Saclay University, INRAE, 78350 Jouy-en-Josas, France

[*]corresponding authors: irina.gutsche@ibs.fr, ambroise.desfosses@ibs.fr

Abstract

Human Respiratory Syncytial Virus (RSV) is a prevalent cause of severe respiratory infections in children and the elderly. The viral genome, enwrapped by the nucleoprotein N into a helical nucleocapsid (NC), is a template for the viral RNA synthesis and a scaffold for the virion assembly. Although the structures of NC filaments representative of the other major families of the *Mononegavirales* order have been solved, a detailed understanding of the RSV NCs is missing. This cryo-electron microscopy (cryo-EM) analysis highlights the polymorphism of the RSV nucleocapsid-like assemblies. We reveal in particular the non-canonical arrangement of the RSV NC helix, composed of 16 N per asymmetric unit, and the resulting systematic variations in the RNA accessibility. We demonstrate that this unique helical symmetry originates from recurring longitudinal interactions by the C-terminal arm of the RSV N, whose truncation abrogates the inter-turn contacts. We report the cryo-EM structures of the full-length helical NC filaments, double-headed NCs, ring-capped NCs and double-decameric N-RNA rings, as well as those of the alternative assemblies formed by a C-terminally truncated N mutant. In addition, we demonstrate the functional importance of the interface involved in the formation of the double-headed and the ring-capped interactions. We put all these findings in the context of the RSV RNA synthesis machinery and delineate the structural basis for its further investigation.

Introduction

Human respiratory syncytial virus (RSV) is the most frequent cause of bronchiolitis and pneumonia in infants and a major cause of childhood death in low-income settings [1,2]. Reinfection can occur throughout life and is often serious in elderly and immunocompromised. Yet, RSV remains one of the only major etiological agents of the lower respiratory tract infections-related mortality for which no licensed vaccine is yet available, with treatment limited to supportive care. Development of effective therapeutics requires a better understanding of the RSV synthesis machinery. RSV belongs to the *Mononegavirales* order with the non-segmented negative strand RNA genome fully coated by the viral nucleoprotein N. The resulting helical nucleocapsid (NC) shields the viral genetic material from recognition by the innate immune system while serving as template for replication and transcription by the viral RNA polymerase complex, thereby constituting a potential drug target.

Alongside RSV and human Metapneumovirus (hMPV), belonging to the *Pneumoviridae* family, *Mononegavirales* contains other important human pathogens such as the *Rhabdoviridae*

rabies, the *Filoviridae* Ebola (EV) and Marburg (MaV), and the *Paramyxoviridae* measles (MeV), mumps (MuV) and Nipah (NiV) viruses. *Pneumoviridae* are equally distant to *Paramyxo-* and *Filoviridae* [3]. In particular, as far as the NCs are concerned (i) each paramyxo- and filoviral N binds precisely 6 nucleotides, whereas pneumoviral N binds 7 [4]; (ii) the genome size of paramyxo- but not pneumo- and filoviruses is a strict multiple of 6 nucleotides; (iii) paramyxo- and filo- but not pneumoviral genomes require bipartite promoters separated by an exact multiple of 6 nucleotides [5]; (iv) paramyxo- and filoviral N possess a very long C-terminal extension involved in replication and transcription, whereas the pneumoviral N features only a short C-terminal arm (*i.e.* the length of MeV N is 525, EV NP 739 and RSV N 391 amino acids respectively) [6]. Removal of the C-terminal extension rigidifies and condenses the helical paramyxo- and filoviral NCs by strengthening the contacts between successive turns, thus facilitating their structural analysis by cryo-electron microscopy (cryo-EM) and tomography (cryo-ET).

Despite a recent massive increase in the number of medium and high resolution cryo-EM structures of the helical paramyxo- and filoviral NCs [7–16], a detailed cryo-EM characterisation of the pneumoviral NCs is still lacking. Here we present an exhaustive cryo-EM analysis of the structural landscape of RSV NCs in solution. We reveal in particular the non-canonical helical symmetry of the RSV NC, with 16 nucleoproteins per asymmetric unit, and demonstrate that this unique organisation results from inter-turn interactions by the C-terminal arm of N and leads to periodic variations in the RNA accessibility along the NC filament.

Results

RSV nucleocapsids are flexible and polymorphic

The current structural information about RSV NCs comes mostly from the 3.3 Å resolution X-ray crystal structure of decameric N-RNA rings [4] (N_{10} ring, PDB: 2WJ8), a negative stain electron tomography analysis of purified helical NCs [17] and two cryo-ET studies of the RSV virion [18,19]. Our cryo-EM images of recombinant RSV N purified from insect cells displayed a polymorphic ensemble in which ring-like particles and filaments could be distinguished and classified (Figure 1a, b). A map of a bottom-to-bottom assembly of two decameric N-RNA rings, termed N_{10} double ring, was derived from the ring-like classes. In parallel, the filaments were split into sets of classes showing either continuous or discontinuous course. The former were used for 3D reconstruction of a helical NC and its ~1.5-turn subsection, whereas the latter yielded reconstructions of a double-headed NC and a ring-capped NC. Thus, five different 3D maps - a double ring, a helical NC and its short subsection, a double-headed NC and a ring-capped NC - were obtained from the same data set (Figure 1c-g; Supplementary Figure 1).

Unique tripartite stabilisation of the RSV N oligomerisation inside a conserved N-hole

The 2.86 Å resolution map and the resulting atomic model of the N_{10} double ring show that the N protomer and the entire N_{10} ring are identical to the crystal structure, with 0.5-Å RMSD over 378 backbone residues and the density of the last twelve residues (380-391) largely disordered. Accordingly, the RNA binding groove formed by the interface between the N-terminal and the C-terminal domains of N (NTD and CTD), and the “4-bases-in, 3-bases-out” RNA conformation remain unaltered.

Similarly to other *Mononegavirales* [20,21], the N- and C-terminal extensions of RSV N, termed NTD-arm (residues 1-36) and CTD-arm (residues 360-391) (Figure 1h), interact with the laterally adjacent N protomers thereby stabilising their oligomeric assembly on the RNA strand by subdomain swapping (Figure 2a). The visible part of the CTD-arm of N_i lies on top of the CTD of N_{i+1} implying that in a helical NC it should be situated in between consecutive turns [4]. In parallel, the NTD-arm of N_{i+1} inserts into a compact fold of the CTD of N_i from the ring interior and extends towards the CTD-arm of N_{i-1}. In this regard, a "latch-bolt type" interaction formed by an insertion of a loop from the NTD of N_{i-1} into an N_i cavity, termed N-hole, has been recently described for paramyxoviral NCs [12,13,21], and is also present in filoviral NCs (Supplementary Figure 2). The structures of RSV and hMPV N_{10} rings [22] (PDB: 5FVC) indicate that pneumoviral NCs do actually possess a cognate N-hole formed by an Supplementary NTD-arm-proximal loop (residues 19-32 in RSV N), together with two short loops from the NTD (86-92) and the CTD (300-307). Likewise, in RSV and hMPV rings, a short loop from the NTD of N_{i-1} (residues 230-238 in RSV N) protrudes into the N-hole of N_i (Figure 2a, b), which demonstrates that the N-hole based interaction is conserved between *Paramyxo-*, *Filo-* and *Pneumoviridae* families (Supplementary Figure 2).

Deeper into the N-hole matter, the first atomic model of an RSV NC helix (PDB: 4BKK), derived from a crystal structure fit into a tomography-based featureless 68-Å pitch spiral, suggested a fascinating direct interaction between three consecutive protomers [17]. Specifically, R234 of N_{i-1} was predicted to bind both D221 of N_i and Y23 from N_{i+1}. Such a tripartite interaction between N_{i-1}, N_i and N_{i+1} does not exist in paramyxo- and filoviral NCs, and to our knowledge has not been explicitly investigated for the hMPV N_{10} ring. Examination of our RSV double ring structure verifies the presence of the tripartite Y23-D221-R234 interaction and shows that it occurs inside the N-hole of N_i which carries D221; the loop 230-238 of N_{i-1} provides R234 while Y23 is contributed by the loop 18-32 of N_{i+1}, whereas Y23 on the equivalent loop of N_i points into the N-hole of N_{i-1} so that to bind R234 of N_{i-2} (Figure 2a). Surprisingly, despite a great resemblance between the RSV and the hMPV N-RNA rings, the latter contains no tripartite contact (Figure 2b). Indeed, although all loops are in place and Y23 is conserved, in hMPV N both D221 and R234 are replaced by serines making the interaction impossible (Figure 2c). Thus, an additional tripartite stabilisation of the "latch-bolt type" interaction seems to be a signature of the RSV NCs.

Molecular determinants of the longitudinal NTD-NTD interaction

In the double ring, the NTD-NTD stacking of two N_{10} rings, whose centers of gravity are 67 Å apart, is assured by D1-symmetry-related β-sheets providing two opposing interacting H100 residues and two R101-E122 hydrogen bonds (Figure 3). Interestingly, examination of the crystal structures of RSV and hMPV rings (Figure 3a-c; Supplementary Figure 3) reveals their bottom-to-bottom (NTD-NTD) stacking but with a tighter packing, with an inter-ring distance of 61 Å and 60 Å respectively. This compaction arises from an inter-ring rotation accompanied by a β-sheet insertion into inter-protomer grooves of the opposite ring (Figure 3a-c), which leads to a difference between the crystallographic inter-ring interface, based on a K91-D96 interaction, and the solution one.

2D classification of segments of filamentous RSV NC produced some 2D class averages featuring a clear seam, either across the filament stem or close to its end (Figure 1b). Particles with the stem-crossing seam yielded a 3.9 Å resolution map with a barbed end-to-barbed end junction of two NC helices (Figure 1e; Supplementary Figure 1), similar to the spiral clams described for *Paramyxoviridae* Sendai (SeV) [13], NiV [23] and Newcastle disease (NDV) [10]. The particles with an

end-proximal seam gave a 3.8 Å resolution map of a helical NC capped by an N_{10} ring (Figure 1d; Supplementary Figure 1), reminiscent of the semi-spiral clam observed for NiV NCs [23]. Remarkably, the mode of the longitudinal NTD-NTD interaction in the double rings, the double-headed and the ring-capped RSV NCs is conserved (Figure 3a, d, e), confirming that the interface delineated by cryo-EM is more reflective of the native structures than the crystal structure interface constrained by the crystal packing. In RSV, the NTD-NTD interface is however distinct from the one in the NiV, SeV and NDV clams, mediated by NTD loops which are absent in pneumoviral N (Supplementary Figure 4).

All *Mononegavirales* NCs are left-handed helices, with the CTDs and the 3'-end of the RNA oriented towards the pointed end of the filaments and the NTDs and the 5'-end towards the barbed ends [20]. The paramyxoviral clam-shaped assemblies were proposed to seed the growth of the double-headed helices from the 5' to the 3' end, protect the 5' end from nucleases [10] and support encapsidation of several NCs per virion [24], also documented for RSV [19,25]. Thus, based on our structures, we designed two double mutants of N – H100E-R101D and H100E-E122R – and assessed their phenotypes in an RSV minigenome assay. While the first construct behaved similarly to the wild type N, the H100E-E122R mutation resulted in a circa 90% reduction of the polymerase activity (Supplementary Figure 5), which suggests a possible functional role of the NTD-NTD interactions in the RSV RNA synthesis.

Cryo-EM analysis reveals a non-canonical symmetry of the helical RSV NC

Although at first glance, the 2D class averages of the RSV NCs with a continuous filament course suggest a paramyxoviral-like arrangement with a herringbone appearance and a ~70 Å pitch, their careful scrutiny shows that every ~1.5 turns (or ~100 Å) densities at either the left- or the right-hand side of the pattern are shifted inwards (Figure 1b; Supplementary Figure 6). The power spectrum (PS) of the 2D classes exhibit an expected layer line with the maximum close to the meridian at ~1/70 Å, attributable to the estimated pitch. Surprisingly however, the PS also features an additional layer line, with a strong maximum on the meridian, at ~1/100 Å, pinpointing a periodicity that should correspond to a ~100 Å rise (Supplementary Figure 6). Since geometrically the rise cannot be larger than the pitch, this implies that the measured value of the rise does not reflect the axial shift between two consecutive protomers. In principle, the ~100 Å periodicity could arise from stacking of short ~1.5-turn helices with a 70 Å pitch; however, no discontinuity and no isolated ~1.5-turn helices were observed in our cryo-EM images despite exhaustive particle picking and extensive 2D classification. Alternatively, if the NCs are continuous, they would be organised in ~1.5-turn asymmetric units composed of multiple N protomers.

3D reconstructions with a 100 Å rise as a starting value and a variable twist led to a solution with correct secondary structures of N, and a subsequent isolation of the straightest NCs yielded a final 3D map at an average resolution of 6.2 Å and a continuous RNA density (Figure 1f; Supplementary Figure 1; Figure 4; Supplementary Figure 6). This moderate resolution lies in the short-range order of the helical RSV NC. Indeed, an additional 3D refinement within a mask enclosing ~1.5 turns resulted in a 3.5 Å average resolution map of a five protomer-subsection in the middle of the mask, which however rapidly deteriorates towards the mask periphery due to a progressive loss of regularity (Figure 1g; Supplementary Figure 1). The structure of the N-RNA protomer is again largely the same as in the crystal, with RMSD less than 1 Å over 378 backbone residues for each of the five protomers, and the inter-protomer contacts maintained.

The determined helical parameters and an inspection of the map and the model of the NC helix (Figure 1f; Supplementary Figure 1; Figure 4a, b) allows to interpret the peculiar experimental class averages and the PS (Supplementary Figure 6). Indeed, the RSV NC reveals itself as a right-handed "super-helix", defined by a 105.3 Å rise and a 149.5° twist, generated by helical repetition of asymmetric units composed of 16 N protomers forming a ~1,5 turns left-handed spiral staircase. Inside each asymmetric unit, the protomer arrangement is similar to that observed in paramyxoviral helical NCs. Amazingly however, the position and the orientation of the protomers relative to the filament axis as well as the axial shift between two consecutive protomers undergo a specific and coordinated variation (Figure 4c). For example, the tilt of the protomers varies between ~40° for the most "standing" (N_6 and N_7) and ~65° for the most "lying" (N_{11}, N_{12} and N_{13}), whereby the most lying subunits are the closest to the helical axis. The combination between the helical parameters and the variation profile of the protomer poses in the asymmetric unit engenders an axial alternation of regions where two neighbouring turns are the closest to each other and regions where they are spread further apart. This alternation occurs circa every 105 Å/1.5 turns/16 protomers and manifests itself by clamping the helix on a side, thereby increasing the gaps above and below the clamps. The helical propagation of the clamps and gaps confers the RSV NC its unique appearance, accentuated by an inward shift of the densities corresponding to projections of the most lying subunits in the 2D class averages (Figure 4; Supplementary Figure 6). The variation of the protomer tilt is visible even on the five protomer-subsection of the helix (Supplementary Figure 1). The numbering of the protomers in the asymmetric unit is done based on the correspondence between their axial tilts in the double-headed NC, where the first barbed-end subunit is clearly identified, and in the helical NC (Supplementary Figure 7).

Periodic variations of RNA accessibility and the CTD-arm-mediated inter-turn interactions in helical RSV NCs

One consequence of this NC organisation is particularly conspicuous: in the configuration where the lower-turn protomers are lying and shifted inwards and the upper-turn protomers standing above, the RNA of the lying protomers is hidden inside the clamps; in contrast, in the standing-protomer configuration the RNA appears exposed (Figure 5). Another striking observation (Figure 5) is that three consecutive "nearly standing" protomers in the lower turn interact with the upper turn through their CTD-arms, which are therefore better defined than in the other protomers where they are not constrained. Indeed, inspection of the CTD-arm densities in the five protomer-subsection and in the entire asymmetric unit shows that the definition of the CTD-arm of each protomer N_i depends on the position and orientation of the protomer(s) located immediately above (*i.e.* N_{i+10}, N_{i+11} and N_{i+12}) (Figure 5). Although modelling of the CTD-arm after the residue 379 [4] would be unreliable, a rigid body fit into the subsection map indicates that the three "nearly standing" subunits of the helical RSV NCs do show densities extending beyond. The CTD-arms of the subunits N_2 and N_3 (equivalent to N_{18} and N_{19} in Figures 4 and 5) seem to contact almost the same zones in the subunits N_{13} and N_{14}, (*i.e*. N_{29} and N_{30}) respectively, whereas the CTD-arm of the subunit N_4 (*i.e*. N_{20}) falls nearly in between the upper subunits N_{14} and N_{15} (*i.e*. N_{30} and N_{31}) because of the singular helical symmetry of the RSV NC (Figure 5).

Shortening of the CTD-arm transforms the RSV NCs into paramyxoviral-like canonical helices

Since the structure of the helical RSV NC demonstrates the involvement of the CTD-arm in the longitudinal contacts, we supposed that shortening of this arm may abrogate inter-turn interactions and thereby transform the non-canonical helix with asymmetric units composed of 16 N arranged in ~1.5 turns into a classical helix with one N per asymmetric unit (Supplementary Figure 6). Considering the previously published data on the major role played by the last 20 residues of N in the RSV polymerase activity and the critical requirement of the N residue L370 for the stabilisation of the N^0P complex [26], we opted for a C-terminally truncated N1-370 construct. The most glaring differences with the cryo-EM images of the full-length (FL) N-RNA were the appearance of two new types of filaments - the herringbone-like helices and a major population of unforeseen rigid stacks of rings (Figure 6; Supplementary Figure 1). The class averages and the PS of the helical NC formed by the N1-370 mutant are similar to those of paramyxoviral NCs, and the helical parameters of the resulting 4.3 Å resolution 3D map, 6.58 Å rise and -36° twist, closely agree with the ones derived from the FL “super-helix” (Supplementary Figure 6). Moreover, the mutant manifests no longitudinal contacts (Figure 6a-c), validating the structure-based hypothesis that it is the CTD-arm of the RSV N that, by periodically linking two successive helical turns, induces the non-canonical symmetry of the RSV NC and the resulting systematic variations in the RNA accessibility.

The rigid polymers coexisting with these helices are D10-symmetric and formed by alternating bottom-to-bottom and top-to-top packing of N_{10} rings (Figure 6d-f). Thus, these stacks are very different from those observed for digested mumps N-RNA rings packed top-to-bottom [12]. The ensuing 2.8 Å resolution cryo-EM map shows that the NTD-NTD stacked units are indistinguishable from the N_{10} double rings of FL N until the end of the α-helix 344-358 and the beginning of the CTD-arm. In the rings and helical assemblies of the FL N, the CTD-arm of the subunit N_i protrudes straight onto the top of the CTD of N_{i+1}. However, in the stacked rings of the N1-370 mutant, the truncated CTD-arm sharply pivots away and, instead of engaging into a lateral interaction, tucks into an identical site but on a CTD of the opposite ring in the stack. The pivoting of all CDT-arms tightly locks the adjacent rings together through their CTDs, such as to generate a polymer built of layers of inversely oriented N_{10} rings engaged both in NTD-NTD and CTD-CTD contacts; the latter are additionally stabilised by binding between CTD-arms of two opposing protomers, in particular through a Y365-Y365 stacking (Figure 6g, h).

Discussion

The major finding of this work was the non-canonical helical organisation of the RSV NC, generated by ~1.5-turn asymmetric units composed of 16 N protomers, which undergo a concerted variation of their poses while remaining in quasi-equivalent environments. This unique symmetry, together with the great flexibility of the NCs, complicates their high resolution analysis, and is totally different from those described for other *Mononegavirales* NCs. Excitingly, the arrangement of the RSV NC is reminiscent of the one proposed for the Dahlemense strain of tobacco mosaic virus (TMV), and may be similarly considered in terms of a periodic deformation of a regular helical structure [27]. In the Dahlemense TMV model, the additional meridional reflexions appear on the layer lines halfway between those of the common TMV and the asymmetric unit contains exactly two turns. Likewise, for the RSV NC the maximum on the meridian is observed at two thirds of the

layer line of the expected pitch and the asymmetric unit contains ~1.5 turns. The exterior distortion proposed in the Dahlemense TMV model is explained by the inside and outside sets of inter-turn interaction being incompatible with the same periodicity, whereas the common TMV does not have any axial outside interactions. The C-terminally truncated RSV NC mutant also has no inter-turn interactions and features a canonical helical symmetry with equivalent environments for each N protomer. In contrast, in the FL NC, the CTD-arms at the filament interior are periodically involved in axial interactions with the upper turn, which induces a global structural reorganisation leading to tilting and inwards shifting of certain protomers and manifesting itself as a helical distortion at the NC exterior. Continuing the parallel, the stability of the observed full-length RSV NC structure would indicate that “the decrease in the free energy upon forming some additional bonds is greater than the increase in the free energy required to move the subunits into the slightly different, but quasi-equivalent positions” [27].

The helical NC, together with the RNA polymerase L, its phosphoprotein cofactor P and the transcription factor M2-1, form the RSV RNA synthesis complex that constitues the minimal infectious unit of the virus. P acts as a central hub by tethering L to the NC template, chaperoning neosynthesised N such as to keep it monomeric and RNA-free (N^0) for specific nascent RNA encapsidation, and recruiting M2-1 [28]. The matrix protein M is thought to direct RSV assembly and budding by interacting both with the NC-bound P and with the envelope glycoprotein F [29,30]. Recent cryo-ET analysis of filamentous RSV virions demonstrated that M is organised in a helical array that would coordinate helical ordering of glycoprotein spikes [19]. In addition, in *Paramyxoviridae*, M was shown to directly bind the CTD-arm of N [31,32]. Thus, RSV M may potentially also influence the helical parameters of the NC upon the viral cycle via a direct or a P-mediated interaction. Noteworthy, the binding pocket of P on the NC helix is situated far both from the CTD-arm itself and from its binding site to the upper helical turn [33,34].

In order to bind M or another viral or host factor, the end of the CTD-arm of N would need to escape outside the NC through an interstice between two turns, as shown for *Paramyxo-* and *Filoviridae,* which however have a much longer CTD extension. Here we showed that the non-canonical helical organisation of the RSV NC is engendered by the last 20 residues of the CTD-arm of N. Considering high similarity between RSV and hMPV N, we suppose that all *Pneumoviridae* NCs adopt an analogous arrangement. Our structures and the structural homology between RSV and hMPV N^0P complexes inferred from biochemical studies [26] suggest that, similarly to the situation in hMPV [22], binding of the N-terminal peptide of RSV P to N^0 would hamper its self-oligomerisation by preventing the CTD-arm from subdomain swapping and flipping it downwards along the core of N such as to block the RNA binding [22]. In contrast, in the stacked N1-370 rings, the truncated CTD-arm rotates upwards to dock into dedicated subdomain swapping site on the opposite N protomer from the ring above. Thus, comparison of these structures indicates that the CTD-arm is able to explore a large angular space (Figure 6i).

While the truncation of the CTD-arm is not supposed to occur *in vivo*, the high rotational freedom of the CTD-arm hints to a possibility of its reorientation upon interaction with viral or host factors. One may therefore envision a temporary capping of the pointed end of the NC helix by an N-RNA ring or a second NC through a CTD-CTD interaction, such as to protect the 3’ end of the RNA from host antiviral responses. This would however imply an uncapping of the 3’ end in order to initiate transcription or replication from the respective promoters that reside at the pointed end of the NC, by either P or L or another factor. The 5’ end, in its turn, would be protected inside the

double-helical and 5' ring-capped NCs formed through NTD-NDT interactions. Such top-to-top and/or bottom-to-bottom assemblies of RSV NCs would be consistent with the observations in the RSV virion [19,25] and in the infected cells [35].

The most obvious consequence of the non-canonical RSV NC structure is the periodic variation of the RNA accessibility, the RNA binding groove of N being severely obstructed in the inwards shifted lying protomers and exposed in the standing ones. While this difference in access to the RNA should inevitably influence pneumoviral synthesis by L during its gliding along the NC, the exact mechanistic implications of the observed variations are difficult to conceptualise. Indeed, because of the limited long-range order of the RSV NC helices, any prediction of the protomer poses based on the numbering in the clam and semi-clam structures as adopted here can only be reliable for the protomers located very close to the barbed, 5'-end. Even an attempt to estimate the tilt of the protomer containing the most 5'-end proximal gene start (GS), at the onset of the gene of L, would be too error-prone. In addition, considering that the CTD-arm is required both for the inter-turn interactions, responsible for the non-canonical NC organisation, and for the prevention of the premature RNA encapsidation by N^0, the mechanisms behind the strong inhibition of the RSV RNA polymerase activity by mutations and truncation of the CTD-arm [26] are certainly convoluted.

Finally, it is essential to keep in mind that *in cellula* the RSV RNA synthesis occurs in virally induced cytoplasmic inclusions considered as active viral factories and formed by liquid-liquid phase separation [36–38]. In line with the structural polymorphism of the purified NCs obtained by heterologous expression described here, we hypothesise that particular functional states of the NCs can be enriched in VFs depending on the progress of the viral cycle or the status of certain cellular pathways. The material properties of biomolecular condensates may also influence the NC structures. Thus, in future it is essential to combine cryo-EM investigation of the structure-function relationships of the RSV synthesis machinery *in vitro* with its cryo-ET analysis in the cellular context.

Methods

Plasmids and baculoviruses

The codon-optimized sequence coding for the wild type (WT) N (stain Long) was synthetised (GenScript) and cloned in the pFastBac Dual vector under the control of the polyhedrin promoter at BamHI and SalI sites. A stop codon was inserted after amino acid residue 370 by site directed mutagenesis using Q5 Site-Directed Mutagenesis Kit (NEB), in order to express the truncated N1-370 construct. Recombinant baculoviruses were recovered using the Bac-to-Bac baculovirus expression system (Invitrogen). N WT or N1-370 bacmids were obtained after transformation of DH10EMBacY bacteria (Geneva Biotech). Recombinant baculoviruses were recovered after transfection of High Five cells using Cellfectin reagent (ThermoFisher Scientific) and amplification.

The plasmid pGEX-PCT (C-terminal residues 161-241 of RSV P protein), used for bacterial expression of the recombinant GST-PCT, has been described previously [39,40]. Plasmids for minigenome assay expressing hRSV N, P, M2-1, and L are designated pN, pP, pM2-1 and pL, and have been described previously [41,42]. The pM/Luc subgenomic minigenome which encodes the firefly luciferase (Luc) reporter gene under the control of the M/SH gene start sequence has also been described [43]. The plasmids encoding N mutants pNH100E, pNH100E-R101D, pNH100E-

E122R, and pN1-370 were generated using Q5 Site-Directed Mutagenesis Kit (NEB). Primers are shown in Supplementary Table 1.

Protein expression and purification

Recombinant GST-PCT was used for purification of recombinant N expressed in insect cells. Briefly, *Escherichia coli* BL21 (DE3) bacteria (Novagen) transformed with the pGEX-PCT plasmid were grown at 37 °C, in 2xYT medium with 100 µg/ml ampicillin. After 7 h, an equal volume of 2xYT medium with 100 µg/ml ampicillin and 80 µg/ml of isopropyl β-d-1-thiogalactopyranoside (IPTG) was added to induce protein expression, before overnight incubation of the culture at 28 °C. Bacteria were harvested by centrifugation at 3000 g for 30 min at 4 °C, resuspended for 30 min in lysis buffer (Tris 50 mM, NaCl 60 mM, EDTA 1 mM, 0.1 % Triton X-100, DTT 2 mM, pH 7.8, anti-proteases (Roche)), and sonicated on ice. Benzonase was then added to the lysate, followed by a 30 min incubation at room temperature. After centrifugation at 10 000 g for 30 min at 4 °C, the supernatant was incubated with Glutathione-Sepharose 4B beads (Cytiva) for 3 h at 4°C. The beads were washed once in the lysis buffer and twice in PBS 1X buffer. Beads were resuspended in PBS 1X and stored at 4 °C.

For expression of N, High Five cells (ThermoFisher Scientific) were infected at a multiplicity of infection of 2 for 72 h with the baculovirus coding either for the WT RSV N or the N1-370 construct. Cells were washed in TEN buffer (50 mM Tris-HCl, 10 mM EDTA, 150 mM NaCl, pH 7.4) and centrifuged at 3000 g for 5 min. The cells were resuspended in 10 ml of lysis buffer (TEN buffer, NP-40 at 0.6 % (v/v), anti-proteases/phosphatases (Roche), RNase (200 µg/ml, Invitrogen), DNase (5 units/ml, Promega)) and incubated 40 min at 37 °C. The lysate was clarified by centrifugation at 14 000 g for 15 min at 4 °C, then incubated for 3 h at 4 °C with the GST-PCT beads previously rinsed in TEN buffer. The GST-PCT beads were then washed once in lysis buffer and twice in TEN buffer and then incubated in TEN buffer in the presence of thrombin (Sigma), for 72 h at 4 °C. The supernatant was collected and concentrated using a column with a MWCO of 100 kDa (Sartorius).

Minigenome assay

BSRT7/5 cells, a cell line derived from the BHK-21 cells, constitutively expressing the T7 RNA polymerase [44], were used for the minigenome assay. Cells were grown in Dulbecco's modified Eagle's medium (Lonza) with 2 mM L-glutamine, antibiotics and 10 % fetal bovine serum. Cells at 90 % confluence in 96-well plate were transfected using Lipofectamine 2000 (Invitrogen) according to manufacturer's instructions with the following plasmid mixture: 62.5 ng of pM/Luc, pP and pN (WT or N mutants), 31.3 ng of p L, 15.6 ng of pM2-1, and 15.6 ng of pRSV-β-galactosidase (Promega) for transfection efficiency normalisation. After 24 h, the cells were lysed in luciferase lysis buffer (30 mM Tris pH 7.9, 10 mM $MgCl_2$, 1 mM DTT, 1% Triton X-100, and 15% glycerol). After addition of the substrate (Luciferase assay system, Promega), the luciferase activities were determined for each cell lysate with an Infinite 200 Pro (Tecan, Männedorf, Switzerland) and normalised based on β-galactosidase (β-Gal) expression. Four replicates were carried out and mean values were calculated. The analysis was done using Excel (Microsoft) and Prism 9 (GraphPad). Expression of WT and mutant N was assessed by Western blot using a rabbit anti-N antiserum [39] and a mouse monoclonal anti-tubulin antibody (Sigma), revealed by incubation with anti-rabbit and anti-mouse antibodies coupled to HRP (SeraCare).

Cryo-EM data collection

3 µL of the purified FL or truncated RSV NC sample were applied to a glow-discharged R2/1 300 mesh holey carbon copper grid (Quantifoil Micro Tools GmbH) and plunge-frozen in liquid ethane using a Vitrobot Mark IV (FEI) operated at 100% humidity at room temperature. Datasets were recorded at the EM platform of the IBS Grenoble, on a Glacios microscope (Thermo Scientific) equipped with a K2 summit direct electron detector (Gatan) operated in counting mode. A summary of cryo-EM data collection parameters can be found in Supplementary Table 2. Movies were acquired with a total dose of 42 $e^-/Å^2$ and a defocus range of -0.7 to -2.4 µm, at 1.145 Å/pixel at the specimen level. Cryo-EM data on the N1-370 mutant was acquired with using beam-tilt induced image-shift protocol (9 images for each stage movement). Micrographs were manually screened based on the presence of particles, amount of contamination and apparent beam-induced movement, resulting in a total of 11,386 selected micrographs for the FL NCs and 6,312 selected micrographs for N1-370 NCs. A visual inspection of the full-length NC dataset showed the presence of at least four types of assemblies – helical NCs, double-headed NCs, ring-capped NCs and double rings – which were processed separately. Similarly, the helical NCs and the stacks formed by the N1-370 mutant were also processed separately.

Image analysis of the non-canonical helical FL RSV NCs

For the helical NCs, an initial manual picking of 800 filaments from a subset of micrographs was performed with EMAN2 e2helixboxer.py [45] and used to create a training dataset for crYOLO [46], which was subsequently used for the picking on all micrographs, resulting in 97,280 filaments traced. The filament coordinates were then used for particle extraction in RELION [47] with a binning to a boxsize of 128 pixels (corresponding to 3.04 Å/pixel) and a 15 Å distance between boxes. A total of 1,406,835 helical segments were picked and iteratively classified in RELION, keeping the straightest 2D class averages at each round, which resulted in 544,972 selected segments. The sum of PS of the aligned segments corresponding to 27 classes selected based on estimated resolution and number of particles was calculated with RELION and inspected with bshow [48], showing a similar pattern for all selected classes. Subsequent processing steps were carried out in cryoSPARC [49]. After estimating the helical rise to ~100 Å from the PS (Supplementary Figure 6), the helical twist was determined on the imported binned segment selection whereby multiple helical 3D refinements were run in parallel using as initial symmetry parameters a fixed 100 Å rise and varying the twist from 60 to 180° with a 10° step. The crystal structure of the RSV N-RNA ring [4] was used to validate the 3D maps after refinement, choose the best one for further analysis and impose the correct handedness. An examination of this intermediate map and of its refined symmetry parameters (~105 Å rise and ~150° twist) enabled us to understand that the helical RSV NC in our cryo-EM images was in fact a right-handed “super-helix”, with an asymmetric unit corresponding to a left-handed helix composed of ~16 adjacent N protomers. Since the rise of this super-helix was larger than the initially defined distance between successive segments, a new template-based picking with the projections of this intermediate map was done in cryoSPARC, using 105 Å as a distance between segments. The picking yielded 769,699 helical segments that were cleaned down to 546,489 particles by further 2D classification. This cleaned particle set was further processed in two different ways. First, it was subjected to a heterogeneous refinement using 5 classes, with no symmetry imposed, in order to select the better resolved and most regular

particles. The three most similar classes were combined into a final set of 389,540 segments that was used for a final helical refinement to an average resolution of 6.2 Å (Fourier Shell Correlation (FSC) at 0.143), which was sharpened with a B-factor of -470 Å^2 for visualisation and rigid body fit of the crystal structure. This map reflects the non-canonical helical RSV NC. Second, because of the flexibility of the super-helix, we decided to focus on one asymmetric unit and performed a refinement with a mask enclosing 16 N protomers created from the helical map. This resulted in a final map, with a subsection of five consecutive well-defined protomers at its centre that had an average resolution of 3.5 Å (FSC at 0.143). The five protomer-subsection map, sharpened with a B-factor of -94 Å^2, was used for subsequent model building and structural analysis.

The variation of the axial shifts between two consecutive protomers and their distances from the helical axis (Figure 4c) was calculated based on the coordinates of the centers of gravity of each protomer obtained from the rigid body-fitted crystal structure. To estimate the tilt of each protomer relative to the helical axis, two Cα atoms (from G106 and H274) were picked on the long inertia axis and the angle between the vector formed by these two atoms and the helical axis was computed.

Image analysis of the double-headed helical NCs and ring-capped NCs

Inspection of the cryoSPARC analysis of the 2D classification from the template-based picking of helical segments, allowed us to identify a 2D class average, corresponding to a class of 10,718 particles, that showed features of a double-headed helix (potentially mixed with ring-capped helices). This class was used for template-based picking, giving a set of 176,614 particles that was iteratively cleaned by 2D classification down to 12,699 particles, mostly by removing double ring side views. From these particles, an *ab initio* reconstruction was calculated, followed by non-uniform refinement, which gave a ~7 Å resolution map used to create templates to re-pick the entire dataset. The resulting over 200,000 particles were classified down to 52,127 particles, with a mixture of classes showing double-headed features and classes showing ring-capped helices. Because the separation between double-headed helices and ring-capped helices by 2D classification only did not seem entirely satisfactory, we imported the particles into RELION and iteratively performed 3D classifications until obtainment of two stable particle subsets (and one subset discarded as junk particles). This procedure resulted in 22,162 particles of ring-capped helices and 25,338 particles of double-head helices. These were imported back into cryoSPARC and used for final non-uniform refinements using the RELION 3D class averages as initial references. The average resolutions (FSC at 0.143) of the resulting 3D reconstructions of the ring-capped and the double-headed helices were 3.9 Å and 3.8 Å respectively; finally, the maps were respectively sharpened with a B-factor of -35 Å^2 and -54 Å^2.

In order to establish the correspondence between the protomers in the double-headed NCs and in the non-canonical helical NCs (and thereby to allow the numbering of the protomers in the asymmetric unit of the non-canonical helix as in Figure 4), we matched each of the 16 rigid body-fitted protomers of the non-canonical NC onto the rigid body-fitted protomers of the double-headed NCs (alignment done on one protomer) and calculated the RMSD between the two structures over five consecutive protomers. The lowest RMSD value (3.39 Å) indicated the register of the N protomers in the double-headed NCs compared to the helical NC.

Image analysis of the RSV N-RNA double rings

In cryoSPARC, manual picking of 50 side views of double rings followed by 2D classification was used to create a 2D template for automatic picking, giving 23,704 particles after cleaning by 2D classification. These particles were used for *ab initio* 3D reconstruction followed by refinement and new particle picking using the refined map projections. Iterative 2D classification gave a set of 57,896 side views. Ring-like top views were not considered because they could potentially correspond to single rings or short helices instead of double rings. The selected side views were cleaned down to 47,212 particles by an additional 3D classification step in order to remove undetected potential C11-symmetric rings or short helices mixed with the C10-symmetric double ring side views. A final non-uniform refinement led to a 3D reconstruction at an average resolution of 2.9 Å (FSC at 0.143), sharpened with a B-factor of -96 Å^2.

Image analysis of the canonical helices formed by the N1-370 mutant

In cryoSPARC, manual picking of 200 helical segments followed by 2D classification was used to prepare templates for the filament tracer job. Two rounds of 2D classification and re-picking were then performed to yield a set of 471,549 helical segments used for initial reconstruction. Different helical symmetries ranging from 9 to 11 subunits per turn with a starting pitch of 60 Å were tested by running multiple helical refinements, and only the refinement starting at 10 subunits per turn gave an interpretable map with visible secondary structures. This map was used to generate 2D projections for a final template-based filament tracer job, which gave, after keeping only the straightest helical segments by iterative 2D classification steps, a final set of 329,706 segments. The last refinement was run with a mask enclosing 30% of the segment length, giving a reconstruction at an average resolution of 4.3 Å (FSC at 0.143), sharpened with a B-factor of -155 Å^2. The refined helical parameters - a -36° twist and a 6.58 Å rise – are very similar to the ones calculated from the helical parameters of the non-canonical helical NC formed by the FL N, assuming one protomer per asymmetric unit (-35.7° twist and 6.58 Å rise).

Image analysis of the N1-370 mutant stack

A 2D class average corresponding to stacked rings derived from an automatic picking of helical segments in cryoSPARC was used for template-based particle picking, followed by 2D classification and re-picking until a stable subset of 81,918 particles was obtained. *Ab initio* 3D reconstruction followed by refinement with imposed D10 symmetry as well as defocus refinement gave a final 3D map at an average resolution of 2.8 Å (FSC at 0.143), which was sharpened with a B-factor of -99 Å^2.

Map visualisation, local resolution calculation, model building and refinement

For all final maps, the local resolution was calculated in cryoSPARC. The most interpretable maps were used for further structural analysis. The crystal structure of the N-RNA monomer (PDB: 2WJ8, chain S) was rigid-body fitted in the maps with Chimera [50]. Where appropriate, refinement was performed using the Phenix software package [51] and manual correction in Coot [52]. At different processing stages, the structures were inspected with Chimera and bsoft [48], and figures were done using ChimeraX [53].

Data Availability

All data presented in this study are included in the published article and its supplementary information, and are available from the corresponding author on request.

Statistics and reproducibility

Data was collected on independent experiments. Statistics details are presented in the Methods section and in the figure legends where appropriate.

References

1. Li, Y. *et al.* Global, regional, and national disease burden estimates of acute lower respiratory infections due to respiratory syncytial virus in children younger than 5 years in 2019: a systematic analysis. *Lancet* **399**, 2047–2064 (2022).

2. Busack, B. & Shorr, A. F. Going Viral—RSV as the Neglected Adult Respiratory Virus. *Pathogens* **11**, 1324 (2022).

3. Afonso, C. L. *et al.* Taxonomy of the order Mononegavirales: update 2016. *Arch. Virol.* **161**, 2351–2360 (2016).

4. Tawar, R. G. *et al.* Crystal structure of a nucleocapsid-like nucleoprotein-RNA complex of respiratory syncytial virus. *Science* **326**, 1279–1283 (2009).

5. Gutsche, I., le Mercier, P. & Kolakofsky, D. A paramyxovirus-like model for Ebola virus bipartite promoters. *PLOS Pathog.* **16**, e1008972 (2020).

6. Jamin, M. & Yabukarski, F. *Nonsegmented Negative-Sense RNA Viruses—Structural Data Bring New Insights Into Nucleocapsid Assembly*. *Advances in Virus Research* **97**, (Elsevier Inc., 2017).

7. Gutsche, I. *et al.* Near-atomic cryo-EM structure of the helical measles virus nucleocapsid. *Science* **348**, 704–7 (2015).

8. Wan, W. *et al.* Structure and assembly of the Ebola virus nucleocapsid. *Nature* **551**, 394–397 (2017).

9. Sugita, Y., Matsunami, H., Kawaoka, Y., Noda, T. & Wolf, M. Cryo-EM structure of the Ebola virus nucleoprotein-RNA complex at 3.6 Å resolution. *Nature* **563**, 137–140 (2018).

10. Song, X. *et al.* Self-capping of nucleoprotein filaments protects the newcastle disease virus genome. *Elife* **8**, 1–19 (2019).

11. Desfosses, A. *et al.* Assembly and cryo-EM structures of RNA-specific measles virus nucleocapsids provide mechanistic insight into paramyxoviral replication. *Proc. Natl. Acad. Sci. U. S. A.* **116**, 4256–4264 (2019).

12. Shan, H. *et al.* Structural plasticity of mumps virus nucleocapsids with cryo-EM structures. *Commun. Biol.* **4**, 1–11 (2021).

13. Zhang, N. *et al.* Structure and assembly of double-headed Sendai virus nucleocapsids. *Commun. Biol.* **4**, 1–10 (2021).

14. Zinzula, L. *et al.* Cryo-EM structure of the cetacean morbillivirus nucleoprotein-RNA complex. *J. Struct. Biol.* **213**, (2021).

15. Fujita-Fujiharu, Y. *et al.* Structural insight into Marburg virus nucleoprotein–RNA complex formation. *Nat. Commun.* **13**, 1–9 (2022).

16. Zhou, K. *et al.* Atomic model of Vesicular Stomatitis Virus and Mechanism of Assembly. *Nat. Commun.* **13**, 5980 (2022).

17. Bakker, S. E. *et al.* The respiratory syncytial virus nucleoprotein-RNA complex forms a left-handed helical nucleocapsid. *J. Gen. Virol.* **94**, 1734–1738 (2013).

18. Liljeroos, L., Krzyzaniak, M. A., Helenius, A. & Butcher, S. J. Architecture of respiratory syncytial virus revealed by electron cryotomography. *Proc. Natl. Acad. Sci. U. S. A.* **110**, 11133–11138 (2013).

19. Conley, M. J. *et al.* Helical ordering of envelope-associated proteins and glycoproteins in respiratory syncytial virus. *EMBO J.* 1–13 (2021).

20. Bloyet, L. M. The nucleocapsid of paramyxoviruses: Structure and function of an encapsidated template. *Viruses* **13**, (2021).

21. Li, T. & Shen, Q.-T. Insights into paramyxovirus Nucleocapsids from diverse assemblies. *Viruses* **13**, (2021).

22. Renner, M. *et al.* Nucleocapsid assembly in pneumoviruses is regulated by conformational switching of the N protein. *Elife* **5**, 1–12 (2016).

23. Ker, D. S., Jenkins, H. T., Greive, S. J. & Antson, A. A. CryoEM structure of the Nipah virus nucleocapsid assembly. *PLoS Pathog.* **17**, 1–19 (2021).

24. Cox, R. M. & Plemper, R. K. Structure and organization of paramyxovirus particles. *Curr. Opin. Virol.* **24**, 105–114 (2017).

25. Loney, C., Mottet-Osman, G., Roux, L. & Bhella, D. Paramyxovirus Ultrastructure and Genome Packaging: Cryo-Electron Tomography of Sendai Virus. *J. Virol.* **83**, 8191–8197 (2009).

26. Esneau, C. *et al.* Biochemical characterization of the respiratory syncytial virus N0-P complex in solution. *J. Biol. Chem.* **294**, 3647–3660 (2019).

27. Caspar, D. L. D. & Holmes, K. C. Structure of dahlemense strain of tobacco mosaic virus: A periodically deformed helix. *J. Mol. Biol.* **46**, 99–133 (1969).

28. Decool, H. *et al.* Interactions between the Nucleoprotein and the Phosphoprotein of Pneumoviruses: Structural Insight for Rational Design of Antivirals. *Viruses* **13**, (2021).

29. Ghildyal, R., Ho, A. & Jans, D. A. Central role of the respiratory syncytial virus matrix protein in infection. *FEMS Microbiol. Rev.* **30**, 692–705 (2006).

30. Bajorek, M. *et al.* Tetramerization of Phosphoprotein Is Essential for Respiratory Syncytial Virus Budding while Its N-Terminal Region Mediates Direct Interactions with the Matrix Protein. *J. Virol.* **95**, (2021).

31. Schmitt, P. T., Ray, G. & Schmitt, A. P. The C-terminal end of parainfluenza virus 5 NP protein is important for virus-like particle production and M-NP protein interaction. *J. Virol.* **84**, 12810–23 (2010).

32. Ray, G., Schmitt, P. T. & Schmitt, A. P. C-Terminal DxD-Containing Sequences within Paramyxovirus Nucleocapsid Proteins Determine Matrix Protein Compatibility and Can Direct Foreign Proteins into Budding Particles. *J. Virol.* **90**, 3650–60 (2016).

33. Galloux, M. *et al.* Characterization of a Viral Phosphoprotein Binding Site on the Surface of the Respiratory Syncytial Nucleoprotein. *J. Virol.* **86**, 8375–8387 (2012).

34. Ouizougun-Oubari, M. *et al.* A Druggable Pocket at the Nucleocapsid/Phosphoprotein Interaction Site of Human Respiratory Syncytial Virus. *J. Virol.* **89**, 11129–11143 (2015).

35. Santangelo, P. J. & Bao, G. Dynamics of filamentous viral RNPs prior to egress. *Nucleic Acids Res.* **35**, 3602–3611 (2007).

36. Rincheval, V. *et al.* Functional organization of cytoplasmic inclusion bodies in cells infected by respiratory syncytial virus. *Nat. Commun.* **8**, 1–11 (2017).

37. Galloux, M. *et al.* Minimal Elements Required for the Formation of Respiratory Syncytial Virus Cytoplasmic Inclusion Bodies In Vivo and In Vitro. *MBio* **11**, (2020).

38. Risso-Ballester, J. *et al.* A condensate-hardening drug blocks RSV replication in vivo. *Nature* **595**, 596–599 (2021).

39. Castagné, N. *et al.* Biochemical characterization of the respiratory syncytial virus P–P and P–N protein complexes and localization of the P protein oligomerization domain. *J. Gen. Virol.* **85**, 1643–1653 (2004).

40. Tran, T.-L. *et al.* The nine C-terminal amino acids of the respiratory syncytial virus protein P are necessary and sufficient for binding to ribonucleoprotein complexes in which six ribonucleotides are contacted per N protein protomer. *J. Gen. Virol.* **88**, 196–206 (2007).

41. Fix, J., Galloux, M., Blondot, M.-L. & Eléouët, J.-F. The Insertion of Fluorescent Proteins in a Variable Region of Respiratory Syncytial Virus L Polymerase Results in Fluorescent and Functional Enzymes But with Reduced Activities. *Open Virol. J.* **5**, 103–108 (2011).

42. Hardy, R. W. & Wertz, G. W. The Product of the Respiratory Syncytial Virus M2 Gene ORF1 Enhances Readthrough of Intergenic Junctions during Viral Transcription. *J. Virol.* **72**, 520–526 (1998).

43. Tran, T.-L. *et al.* The Respiratory Syncytial Virus M2-1 Protein Forms Tetramers and Interacts with RNA and P in a Competitive Manner. *J. Virol.* **83**, 6363–6374 (2009).

44. Buchholz, U. J., Finke, S. & Conzelmann, K. K. Generation of bovine respiratory syncytial virus (BRSV) from cDNA: BRSV NS2 is not essential for virus replication in tissue culture, and the human RSV leader region acts as a functional BRSV genome promoter. *J. Virol.* **73**, 251–9 (1999).

45. Tang, G. *et al.* EMAN2: an extensible image processing suite for electron microscopy. *J. Struct. Biol.* **157**, 38–46 (2007).

46. Wagner, T. *et al.* SPHIRE-crYOLO is a fast and accurate fully automated particle picker for cryo-EM. *Commun. Biol.* **2**, 218 (2019).

47. Scheres, S. H. W. RELION: implementation of a Bayesian approach to cryo-EM structure determination. *J. Struct. Biol.* **180**, 519–30 (2012).

48. Heymann, B. J. Bsoft: Image Processing for Structural Biology. *Bio-protocol* **12**, e4393 (2022).

49. Punjani, A., Rubinstein, J. L., Fleet, D. J. & Brubaker, M. A. cryoSPARC: algorithms for rapid unsupervised cryo-EM structure determination. *Nat. Methods* **14**, 290–296 (2017).

50. Pettersen, E. F. *et al.* UCSF Chimera--a visualization system for exploratory research and analysis. *J. Comput. Chem.* **25**, 1605–12 (2004).

51. Adams, P. D. *et al.* PHENIX: a comprehensive Python-based system for macromolecular structure solution. *Acta Crystallogr. D. Biol. Crystallogr.* **66**, 213–21 (2010).

52. Emsley, P., Lohkamp, B., Scott, W. G. & Cowtan, K. Features and development of Coot. *Acta Crystallogr. D. Biol. Crystallogr.* **66**, 486–501 (2010).

53. Goddard, T. D. *et al.* UCSF ChimeraX: Meeting modern challenges in visualization and analysis. *Protein Sci.* **27**, 14–25 (2018).

Acknowledgements

We thank Julien Sourimant for providing the pFastBac-N plasmid, Guy Schoehn for establishing and managing the IBS cryo-electron microscopy platform and for providing training and support, Lefteris Zarkadas for assistance at the Glacios microscope and Daphna Fenel and Emmanuelle Neumann for assistance at the negative stain EM platform. This work was funded by the Agence Nationale de la Recherche (grant ANR DecRisp ANR-19-CE11-0017-01). We used the platforms of the Grenoble Instruct-ERIC center (ISBG; UAR 3518 CNRS-CEA-UGA-EMBL) within the Grenoble Partnership for Structural Biology (PSB), supported by FRISBI (ANR-10-INBS-0005-02) and GRAL, financed within the University Grenoble Alpes graduate school (Ecoles Universitaires de Recherche) CBH-EUR-GS (ANR-17-EURE-0003). The EM facility is supported by the Rhône-Alpes Region, the Fondation Recherche Medicale (FRM), the fonds FEDER and the GIS-Infrastrutures en Biologie Sante et Agronomie (IBISA). LG acknowledges the financial support by the ANR (DecRisp ANR-19-CE11-0017-01) and the Fondation pour la Recherche Médicale (FRM, FDT202204015081).

Author contributions

LG, MBV, DC, MG and IG performed experiments, LG, AD and IG analysed the cryo-EM data. LG, JFE and MG analysed the biological data. IG and JFE designed the overall study. IG, AD, JFE and MG supervised the project. IG wrote the manuscript with contributions of LG, AD, MG and JFE. LG, AD and IG prepared the figures. All authors read the manuscript prior to submission.

Competing Interests: The authors declare that there are no competing interests.

Figures and Legends

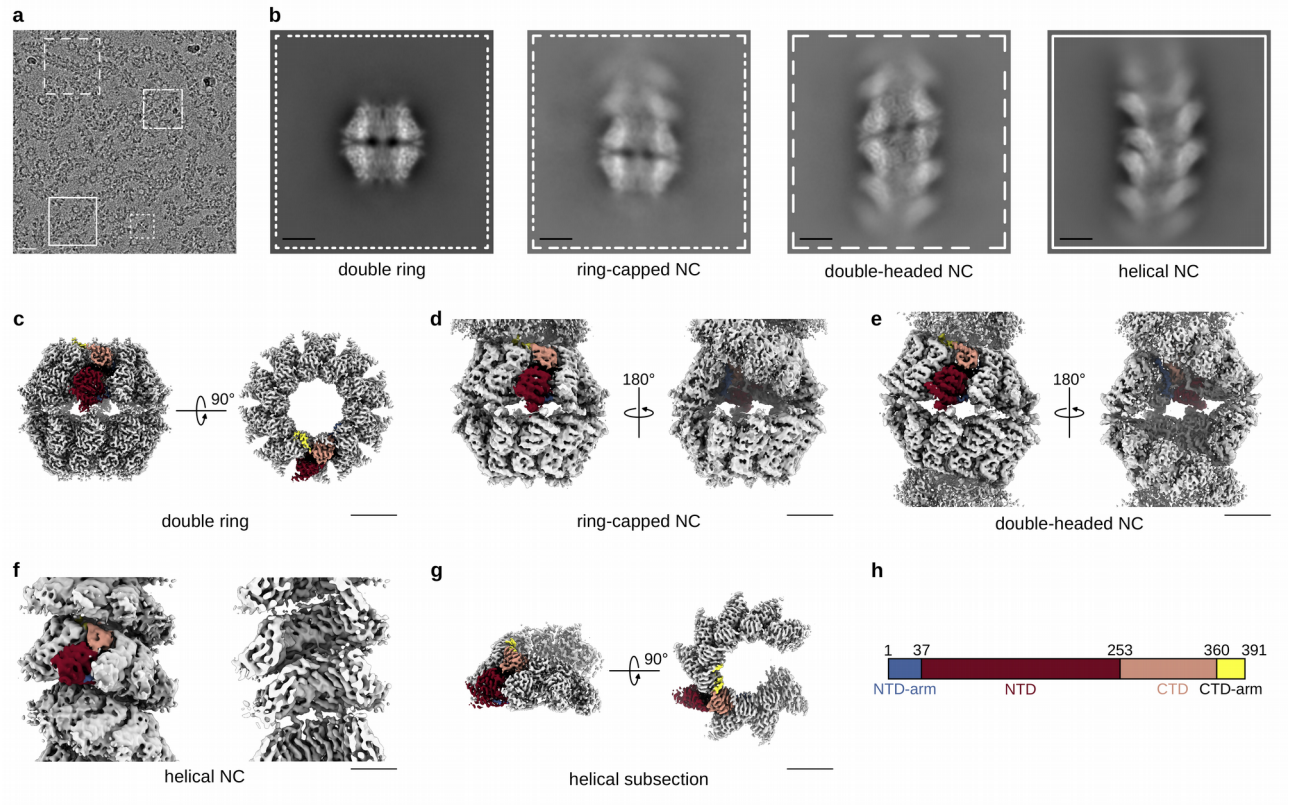

Figure 1: **Cryo-EM analysis of RSV NCs.** (a) A representative micrograph of RSV NCs purified from insect cells and featuring double rings, ring-capped NCs, double-headed NCs and helical NCs. Particles are boxed as an illustration, scale bar 200 Å. (b) Representative 2D classes with the outline matching the particles highlighted in (a). (c) Cryo-EM map of the N_{10} double ring (side and top view). (d) Cryo-EM map of the ring-capped NC (front and back view). (e) Cryo-EM map of the double-headed NC (front and back view). (f) Cryo-EM map of the helical NC (front and cut-through view). (g) Helical subsection (side and top view). Scale bar, 50 Å in (b-g). (f) Schematic of the RSV N sequence divided into an NTD-arm (blue-gray), NTD (rosewood), CTD (old rose) and CTD-arm (yellow). In cryo-EM maps in (c-g), one protomer is coloured according to this schematic, with the RNA in black.

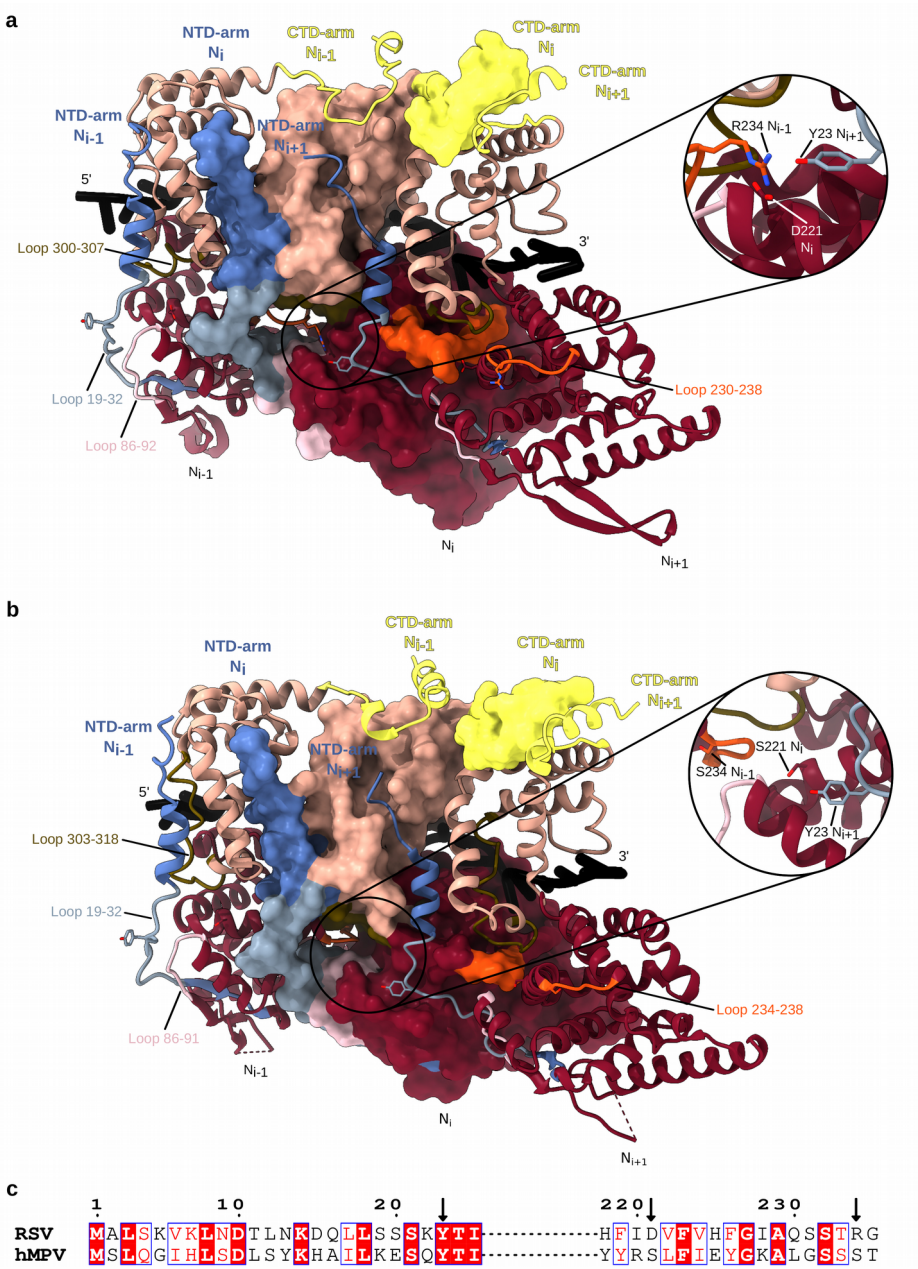

658 **Figure 2**: **Lateral interactions between N protomers in RSV and hMPV N_{10} double rings**. (a)
659 Atomic models of three consecutive RSV N protomers are shown, the middle one as a surface and
660 the edge ones as ribbons. NTD-arm, NTD, CTD and CTD-arm coloured as in Figure 1, loop 19-32
661 in powder blue, loop 86-92 in mimi pink, loop 230-238 in orange and loop 300-307 in olive. The
662 close-up of the N-hole of the middle protomer shows the tripartite Y23-D221-R234 interaction. (b)
663 Same as (a) but for three protomers from the hMPV N-RNA ring crystal structure (PDB: 5FVC).
664 Colouring as in Figure 1 and in (a), loop 19-32 in powder blue, loop 86-91 in mimi pink, loop 234-
665 238 in orange and loop 303-318 loop in olive. The close-up shows the absence of a tripartite
666 interaction in the N-hole. (c). Pairwise sequence alignment of RSV and hMPV N around the
667 residues involved in the tripartite interaction in the RSV N oligomer. Conserved residues in red
668 boxes; arrows pointing at residues 23, 221 and 234.

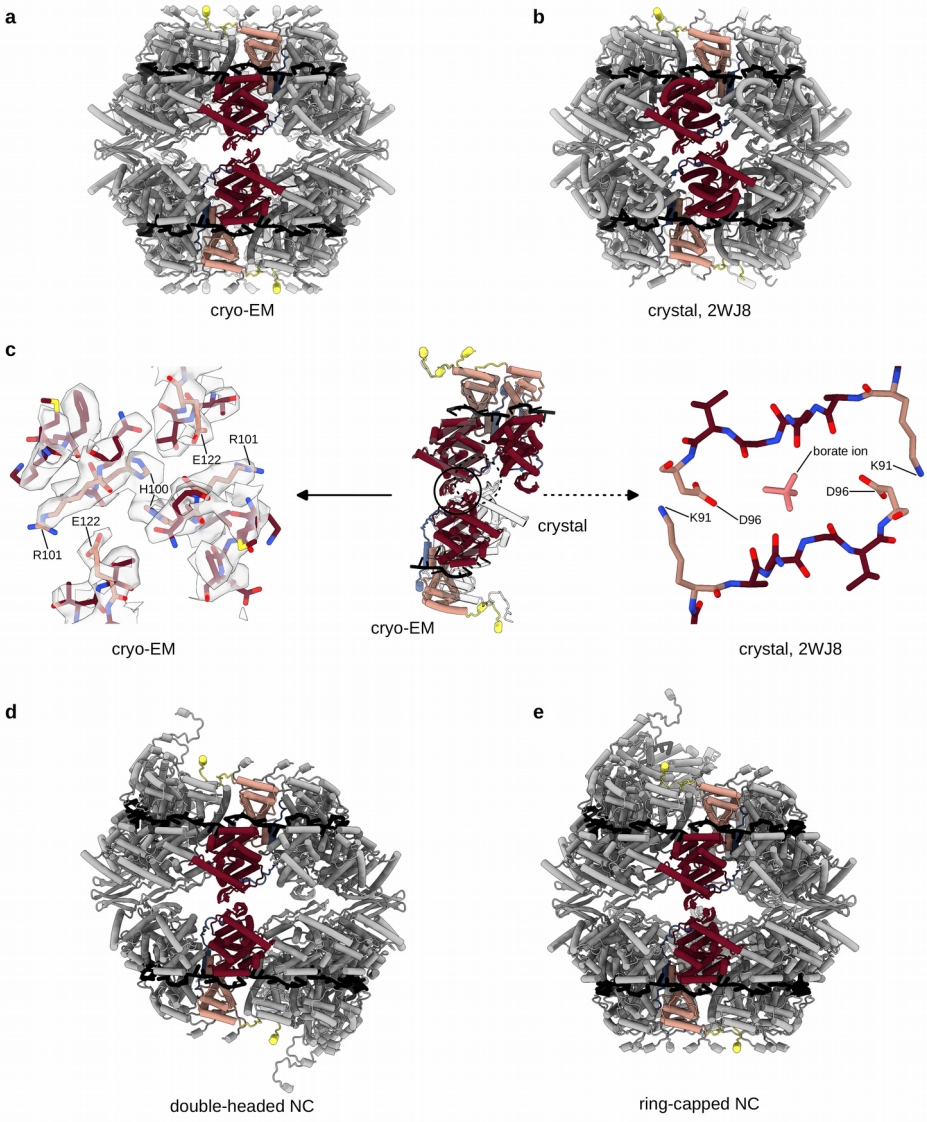

669 **Figure 3. Longitudinal NTD-NTD interactions conserved between RSV N_{10} double ring,**
670 **double-headed and ring-capped NCs but different from the crystal structure of the RSV N_{10}**
671 **double ring.** In each panel, two opposite protomers are coloured as in Figure 1. (a) Atomic model
672 of the RSV N_{10} double ring derived from the cryo-EM map shown as cartoon. (b) Atomic model of
673 the RSV N_{10} double ring crystal structure (PDB: 2WJ8). (c) Alignment of the top rings of the cryo-
674 EM and crystal structure-based models reveals a rotation between the bottom rings. Two top-ring
675 protomers and one opposing bottom-ring protomer are shown in the middle of the panel, with the
676 cryo-EM-based structure coloured as in Figure 1 and the crystal structure in white. A close-up of
677 the cryo-EM map and the atomic model highlighting the NTD-NTD interactions is on the left, a
678 close-up of the NTD-NTD interactions in the crystal structure is on the right. The difference
679 between the crystallographic and the solution inter-ring interfaces may be related to the presence
680 of a borate ion in the interaction site in PDB: 2WJ8, possibly embarked during the electrophoretic
681 separation of decameric and undecameric RSV N-RNA rings prior to crystallisation. (d) Atomic
682 model of the double-headed NC. (e) Atomic model of the ring-capped NC.

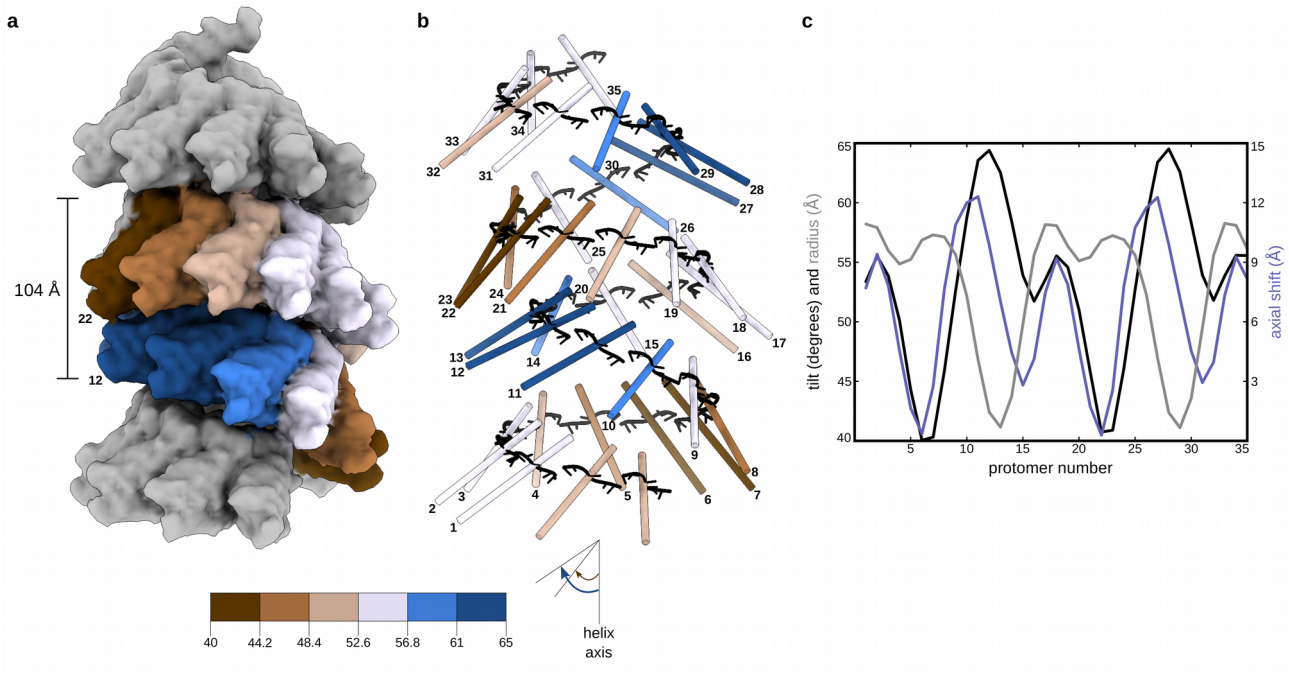

683 **Figure 4**. **Non-canonical helical symmetry of the RSV NC.** (a). Atomic model of the NC is
684 filtered to 10 Å resolution and displayed as surface. Protomers in one asymetric unit are coloured
685 dependent on their axial tilt following the colour code shown at the schematic underneath, the rest
686 of the protomers are coloured in grey. (b). Protomers of the model in (a) are shown as sticks
687 coloured dependent on the protomer axial tilt and numbered 1 to 35. (c) Plot showing the axial tilt
688 (black), the radial position (grey) and the relative axial shift of each protomer.

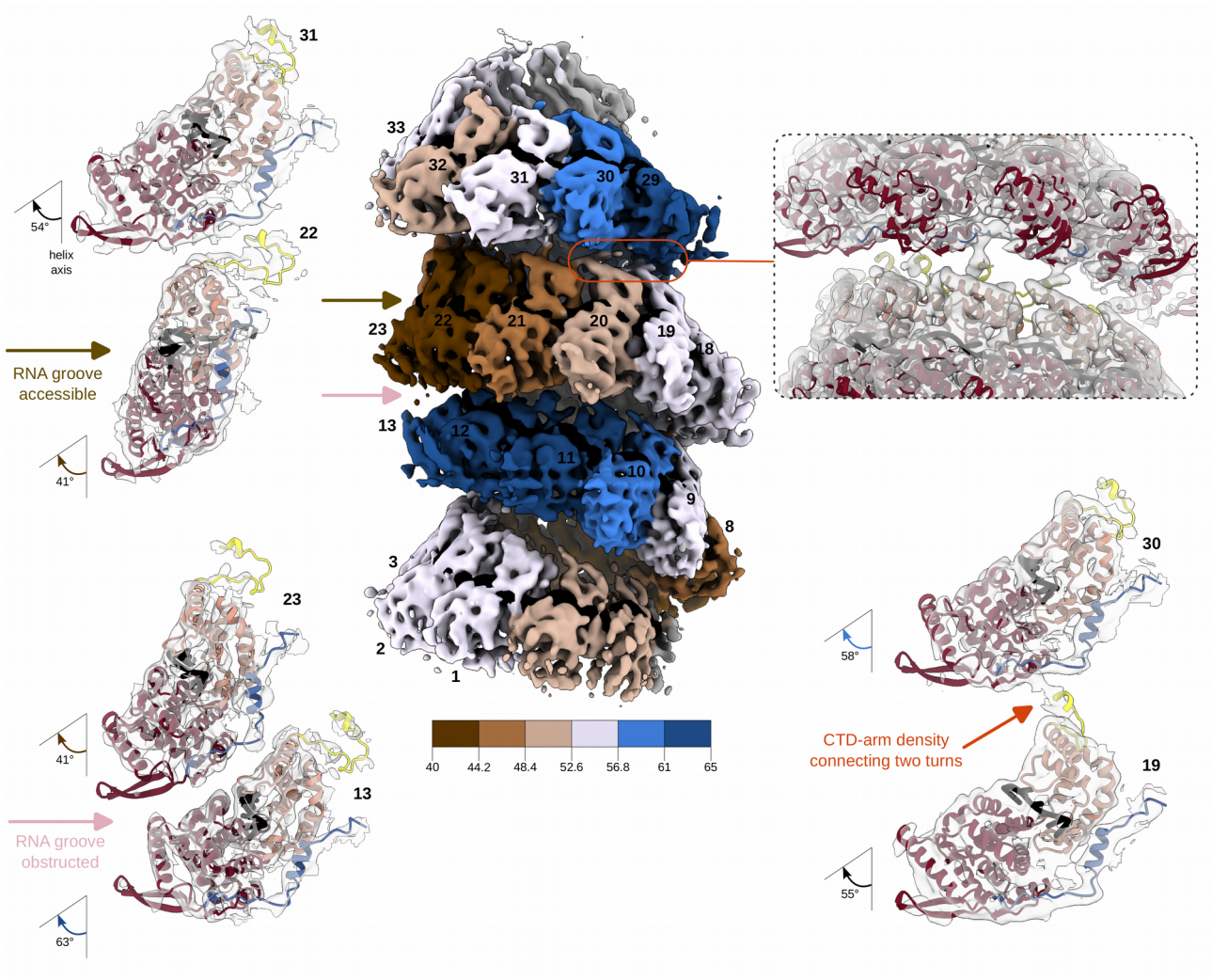

689 **Figure 5**. RNA accessibility and CTD-arm-mediated inter-turn interactions in the helical NC. Cryo-
690 EM map of the helical NC is shown in the middle, coloured as in Figure 4 and as reminded in the
691 schematic underneath the map, with protomers numbered as in Figure 4. On the left, close-up
692 views of two sets of opposing protomers from two successive helical turns are shown to illustrate
693 the difference in the RNA accessibility, with the cryo-EM density in transparent grey and the atomic
694 model represented as a ribbon and coloured as in Figure 1. On the top right, a similarly-coloured
695 view of the inter-turn interaction is shown to highlight the densities corresponding to the CTD-arm,
696 with a corresponding two-protomer close-up underneath. RNA is in black.

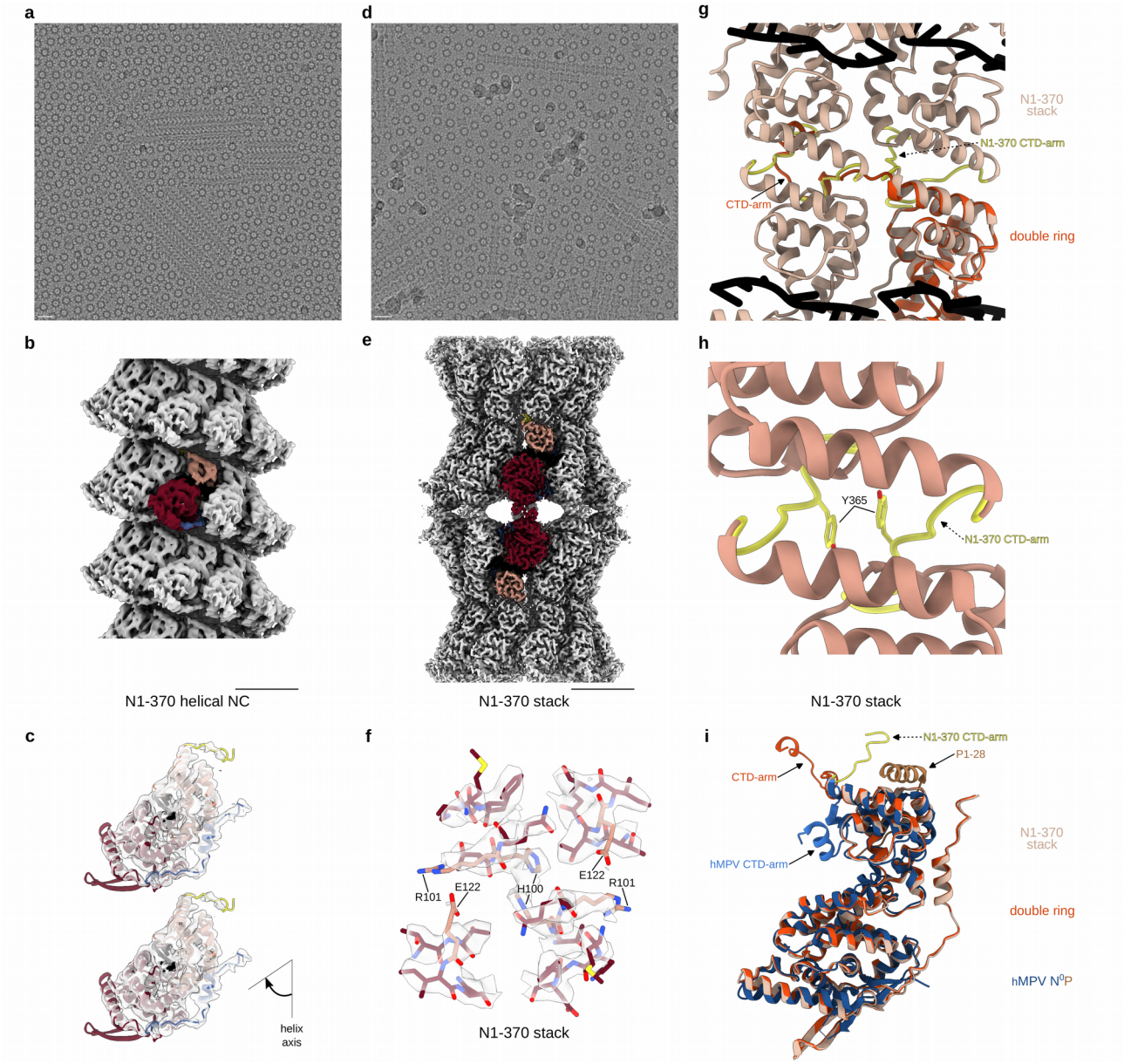

Figure 6. Canonical helical NCs and stacked assemblies formed by the N1-370 mutant. (a) A representative micrograph of the N1-370 NCs featuring mostly helical NCs and rings, scale bar 200 Å. (b) Cryo-EM map of the canonical N1-370 helical NC, with one protomer coloured as in Figure 1, scale bar 50 Å. (c) Close-up view of protomeres from two successive helical turns are shown to illustrate the position of the CTD-arm and the absence of inter-turn interactions, with the cryo-EM map in transparent grey and the atomic model represented as a ribbon and coloured as in Figure 1. (d) A representative micrograph of the N1-370 NCs featuring mostly stacks and rings, scale bar 200 Å. (e) Cryo-EM map of the N1-370 stack, with one protomer coloured as in Figure 1, scale bar 50 Å. (f) Close-up of the cryo-EM map of the N1-370 stack and the atomic model highlighting the NTD-NTD interactions (similar to the ones in the N_{10} double ring shown in Figure 3c). (g) Alignment of the atomic models of the N_{10} double ring and the N1-370 stack illustrating the difference in the orientation of the CTD-arms. One protomer of the N_{10} double ring is shown in the bottom-right and coloured in orange, 4 protomers of the N1-370 stack are shown and colored in beige, with the

710 CTD-arms in yellow. RNA is in black. (h) Close-up of the atomic model of the N1-370 stack
711 highlighting the CTD-CTD interactions. (i) Alignement of N protomeres of the N_{10} double ring
712 (orange), the N1-370 stack (beige) and the hMPV N^0P crystal structure (N^0 in blue and P1-28 in
713 brown) (PDB: 5FVD). Positions of the CDT-arms are indicated.